Basin testing of the 1-2-1 M4 wave energy converter

Damon Howe, Benhur Joseph Raju, Christine L. Hansen, Hugh Wolgamot, Adi Kurniawan, Jean-Roch Nader, Chris Shearer, and Peter Stansby

Abstract—**The M4 wave energy converters consist of three rows of floats, with the front two rows rigidly connected and a hinged connection(s) to the back row. The various possible configurations are commonly identified by the number of floats in each row—hence 1-2-1 has 1 float in front, 2 in the middle, and 1 at the rear. A previous study showed that the 1-2-1 and 1-3-2 variants had the lowest cost of energy of all configurations studied. The 1-3-2 variant has subsequently been extensively studied as it provides greater power per machine. However, the 1-2-1 device has received less attention. In this paper, we report, for the first time, wave basin testing of a 1-2-1 variant. The design is a 1:15 scaled version of a 1-2-1 M4 suitable for deployment in the prevailing short-period wind waves in King George Sound, Albany, on the south coast of Western Australia. The tests were carried out in the Model Test Basin at the Australian Maritime College, Tasmania. Decay tests, regular waves and irregular operational and extreme seas were tested. Body displacements, mooring loads, run-up on the middle floats and forces in the PTO (where installed) were measured. Measured motions were compared to a linear model, with natural frequencies, mooring stiffness and PTO characterisation also explored. Implications of the test results for deployment in King George Sound are discussed.**

Index Terms—**articulated, laboratory experiments, wave energy converter.**

I. Introduction

THE Moored MultiMode Multibody wave energy converter, commonly known as M4, uses multiple floats responding in multiple modes to enhance energy capture. It combines the principles of point-absorber and hinged-raft converters to couple heave, surge and pitch excitation to enhance energy extraction performance.

The M4 differs from other multi-float and hinged WECs such as the Sea Power design [1] by using truncated cylindrical floats with hemispherical bases instead of rectangular floats to minimise material requirements and losses due to drag effects. The floats are arranged in increasing diameter and draft from bow to stern, allowing the device to naturally weathervane from a single point mooring to align itself to the incident waves. The bow float and the mid floats are rigidly joined to a connecting frame, while the aft float along with the aft frame is connected to the forward body through hinges coupled with the power take-off (PTO) system. Power is obtained from the rotational motion generated by the relative pitching of the forward and aft arms.

The design principles of the M4 device are well explained by Stansby et al. [2]. Initially, the floats were arranged longitudinally with the same spacing, equal to half the wavelength of the predominant wave. Later, it was found that increasing the spacing between the mid float and bow float by more than half the length between the aft float and mid float produced more power [3].

A study conducted by Stansby et al. [4] to see the influence of extending the number of floats and its arrangements in different configurations showed that increasing the number of floats from 3 to 8 increased the power capacity significantly. However, considering the Levelized Cost of Energy (LCoE), 6 float 1-3-2 and 4 float 1-2-1 devices were found to be more advantageous. (Here X-Y-Z configuration means X floats in the bow row, Y floats in the middle row and Z floats in the aft, each on separate articulated arms). Experimental studies of 3 float M4 devices [5], [6] and 6 float devices are available [7]. However, the 1-2-1 configuration of M4 has not been extensively studied to date.

Funded by the Blue Economy CRC and Western Australian Government, Marine Energy Research Australia (MERA) are leading a program to deploy a 1-2-1 M4 WEC approximately 20 m in length in King George Sound, Albany on the south coast of Western Australia. The Sound is protected from much of the Southern Ocean swell, but exposed to predominant Easterly winds during summer which generate windseas which can excite an M4 of this size. Further details on the site can be found in Kurniawan et al. [8]. Basin testing forms a crucial part of the development of this project, enabling sea-states chosen to represent the deployment site to be tested, and responses measured

This research was supported by the Blue Economy Cooperative Research Centre through the project 'Seeding Marine Innovation in WA with a Wave Energy Deployment in Albany'. The Blue Economy Cooperative Research Centre (CRC) is established and supported under the Australian Government's CRC Program, grant number CRC-20180101. This research was also supported by Marine Energy Research Australia, jointly funded by The University of Western Australia and the Western Australian Government, via the Department of Primary Industries and Regional Development (DPIRD). HW and CLH were supported by the ARC Early-Career Fellowship DE200101478.

D. Howe, B. Joseph Raju and J-R. Nader are with National Centre for Maritime Engineering and Hydrodynamics, Australian Maritime College, University of Tasmania, Locked Bag 1395, Launceston, Tasmania, Australia (e-mail: damon.howe@utas.edu.au).

C. L. Hansen, H. Wolgamot and A. Kurniawan are with the Oceans Graduate School, University of Western Australia, Crawley, WA 6009 and Marine Energy Research Australia (MERA).

Peter Stansby is at the School of Engineering, University of Manchester.

Chris Shearer is at BMT, Australia.

Digital Object Identifier: https://doi.org/10.36688/ewtec-2023-522

for comparison with numerical models and design assumptions.

II. Experimental setup

A. Experimental model

The 1-2-1 M4 device has 1 float in the bow, 2 floats in the middle and 1 float at the aft. This is a 1:15 scale model of the prototype M4 device that will be deployed in King George Sound. The model has an overall length of 1.6 m and the mid-section is the widest point with a width of 0.634 m. The floats of the model were made with 3 layers of 450 GSM double bias fibreglass, while the triangular frames connecting the floats were made with 2 layers of 300 GSM prepreg carbon fibre laid over 80 kg/m^3 PVC foam. The important physical dimensions of the model compared to the prototype are given in Table I. Ballast is required, at model and prototype scales, to achieve these values.

TABLE I
Physical parameters of the model compared to the prototype

Model Parameters	Model	Prototype
Scale	1	15
Water Depth [m]	0.8	12
Length (bow float to mid float) [m]	0.89	13
Length (mid float to aft float) [m]	0.53	8.0
Length (bow float to aft float) [m]	1.4	21
Width (mid float to mid float) [m]	0.47	7.0
Diameter (bow float) [m]	0.13	2.0
Diameter (mid floats) [m]	0.17	2.5
Diameter (aft float) [m]	0.23	3.5
Draught (bow float) [m]	0.14	2.1
Draught (mid floats) [m]	0.14	2.1
Draught (aft float) [m]	0.15	2.3
Hawser Length [m]	1.3	20
Estimated Natural Heave Period [s]	0.76	2.9
Estimated Natural Roll Period [s]	0.89	3.4
Estimated Natural Pitch Period [s]	0.77	3.0
Estimated Natural Flex Period [s]	0.84	3.2
Mass (total) [kg]	11.4	38500

*All length and width measurements are centre-to-centre.

A picture of the model operating in the basin with the PTO engaged can be found in Fig. 1, where both global and focused camera views can be observed. A top view schematic of the model is shown in Fig. 2 and the side view schematic of the model is shown in Fig. 3, both of which illustrate the global coordinate system datum at the keel of the centre floats aligned with the longitudinal axis of the model.

1) Model mass properties: The total mass of the model after fabrication was 4.49 kg. Additional masses were fitted inside the floats to adjust the mass and draught of the model to the scaled values. The centres of gravity of the forward and aft bodies are measured relative to the datum illustrated in Fig. 2 and Fig. 3. The targeted model scale centres of gravity for the forward and aft bodies relative to this datum are given in Table II.

In order to match the experimental centres of gravity with the targeted values, inclination tests and bifilar

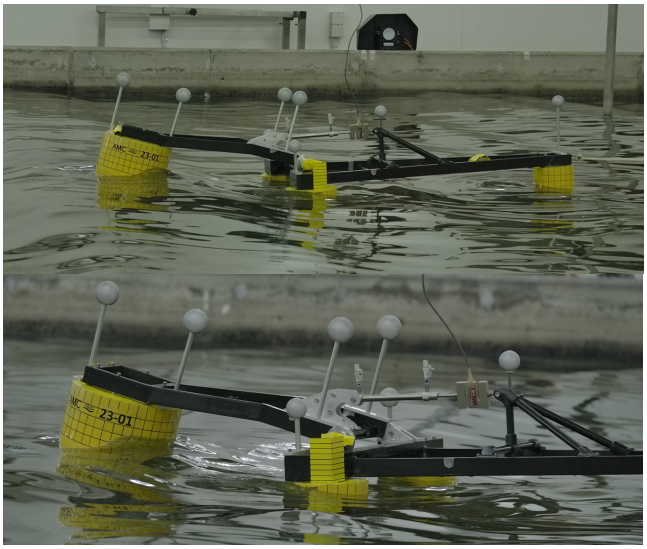

Fig. 1. Global (top) and focused (bottom) views of M4 model operating in OSS 5 within the Australian Maritime College Model Test Basin.

TABLE II
Desired centre of gravity locations for forward and aft bodies

	Forward Arm	Aft Arm
x [m]	0.230	-0.497
y [m]	0.001	0
z [m]	0.185	0.087

tests were carried out. Inclination tests were performed to find the vertical centres of gravity (VCG) of the forward part and the whole model. The forward part consists of the bow float, mid floats and the triangular frame that connects these floats. Masses were transferred vertically within the model to adjust the VCG to the desired value following each iteration of the inclining tests. The final values of the VCG compared to the desired are shown in Table III, where the VCG is measured from the keel of the mid-floats.

TABLE III
Vertical centre of gravity for the model

Parameter	Forward Arm	Whole Model
KG [m]	0.196	0.143
Desired KG [m]	0.185	0.140
Difference [%]	5.72	2.36

After adjusting the VCG, bifilar tests were performed to adjust the moment of inertia of the forward part and the whole model. The model was strapped to a bifilar beam attached to the ceiling in such a way that the centre of the bifilar beam could be aligned with the centre of the body and along the axis of rotation of the required moment of inertia. The body was then oscillated along the axis of rotation and the moment of inertia of the body calculated by estimating the period

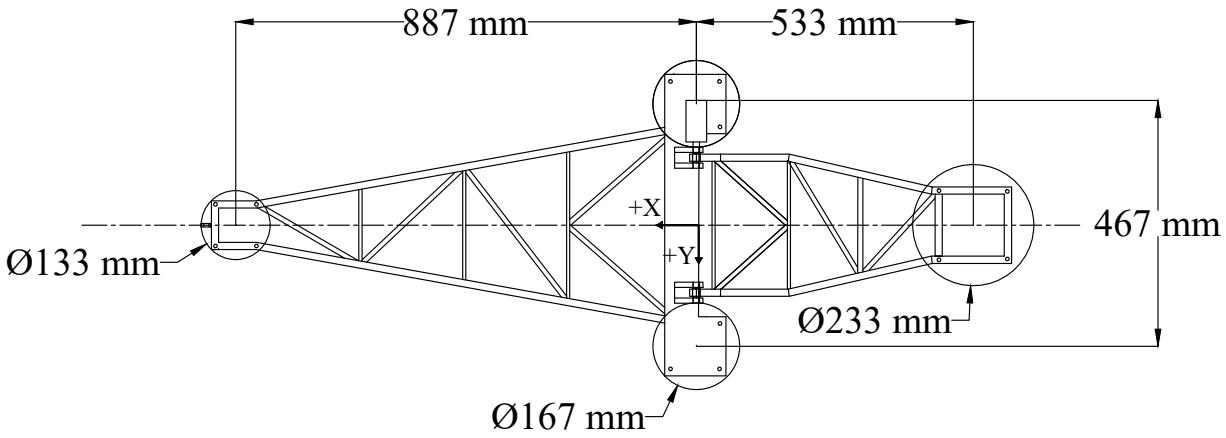

Fig. 2. Top view of the M4 model.

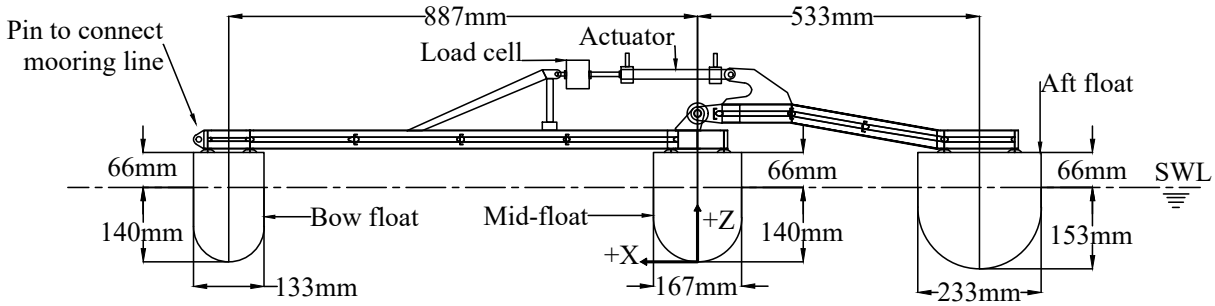

Fig. 3. Side view of the M4 model.

of these oscillations using

$$I = \frac{mgl^2}{h}\left(\frac{T}{2\pi}\right)^2. \quad (1)$$

Here T is the period of oscillations, m is the total mass of the swinging body including the mass of the bifilar beam and the straps used to attach the body to the beam, l is the half-length between the supporting cables, and h is the vertical height the body is hanging from the fixed support (ceiling). The bifilar beam had a mass of 1.444 kg and two straps with a total mass of 0.193 kg were used for attaching the model. The beams were hung using stainless steel cables at a height 1.845 m from the ceiling and with 1.213 m separation between the cables.

The moments of inertia for pitch and roll of the forward part and the whole model were adjusted by shifting the positions of the attached weights on the model until a value closest to the desired scaled value was obtained. The moment of inertia values compared to the scaled value are given in Table IV.

2) Power take-off system: A description of the power take-off to be used in the prototype is given by Apsley et al. [9].

In the model tests, the power take-off was simulated using a pneumatic actuator (SMC CD85N12-100C-B) connected in line with an Xtran S1W-250 load cell.

The actuator was selected to provide a damping force of approximately the appropriate magnitude, given the velocity of relative motion between the bod-

TABLE IV
MASS MOMENT OF INERTIA FOR THE MODEL, WITH RESPECT TO THE CENTRE OF GRAVITY

Parameter	Pitch	Roll
MOI for Forward Arm [kg·m^2]	0.813	0.298
Desired MOI for Forward Arm [kg·m^2]	0.813	0.290
MOI for Whole Model [kg·m^2]	2.215	0.304
Desired MOI for Whole Model [kg·m^2]	2.453	0.297

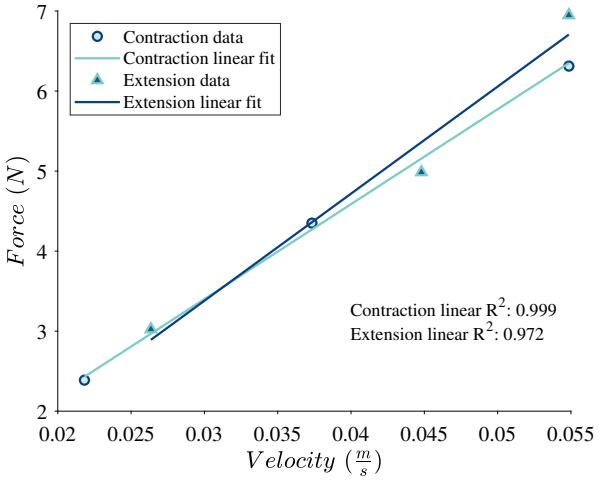

Fig. 4. Pre-testing characterisation of pneumatic actuator linear damping properties.

ies attached at either end. This force was characterised pre-testing by applying known weight forces to the end of the piston and observing the rate of displacement achieved. It was characterised for both extension and contraction of the piston and the fitted linear damping coefficients found were 121.6 N·s/m for the extension and 130.66 N·s/m for the contraction. Fig. 4 illustrates the characterisation of the actuator prior to basin testing across a range of applied loads, where it can be seen that a reasonable linear relationship was observed with the coefficient of determination returned being greater than 0.97.

3) Experimental mooring configuration: In the prototype the mooring involves a 20 m long double hawser system connected to a mooring buoy, which is then moored to the seabed by a catenary system.

To reduce the complexity of the experimental investigation, the full-scale mooring arrangement was simplified to a representative linearised restoring force, which was provided during experiments by a thin latex elastic band of width 38 mm. The linearity of the band's restoring force was calculated by adding known weights to one end of vertically suspended band and measuring its elongation. The selected band had an elasticity of 6.12 N/m (see Fig. 5).

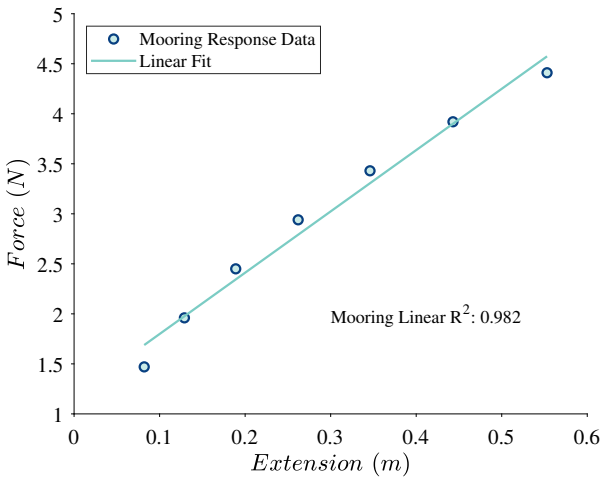

Fig. 5. Pre-testing characterisation of elastic mooring simulant.

The length of the mooring band matched the scaled length of the mooring hawser on the prototype and was attached to a fixed point within the test basin. To measure the mooring loads, the band was connected to a small inline load cell (Futek LSB210). The model was also fitted with a rear mooring line attached to the model using a bridle, which was connected to a known mass suspended via a pulley arrangement, designed to keep tension in the mooring band and keep the model aligned at 0° incidence to the incoming waves.

B. Experimental test matrix

The experimental testing campaign consisted of four main conditions across which the device was subjected to a variety of regular and irregular sea states (all longcrested). The conditions included within the experimental test campaign, and the governing parameters, can be found in Table V, while the regular and irregular sea states tested are specified in Tables VI and VII respectively. The sea states have been chosen based on the joint probability diagram constructed from measurements collected at the King George Sound site [8]. It should also be noted that a series of design waves were tested, the details of which can be found in [10].

TABLE V
CONDITION PARAMETERS FOR BASIN TESTING OF M4 WEC

Condition	Control Variable	Parameters
1	Wave Calibration	Model Removed from Basin
2	PTO Engaged	Waves: Regular and OSS Heading: 0° Incidence
3	PTO Disengaged	Waves: OSS and ESS Heading: 0° Incidence
4	15° Heading	Waves: OSS and ESS

TABLE VI
REGULAR WAVE PARAMETERS TESTED DURING BASIN EXPERIMENTS

Regular Wave Parameters	full
T [s]	2.71, 3.10, 3.49, 3.87, 4.26, 5.42, 6.97
H [m]	0.6
	model
T [s]	0.7, 0.8, 0.9, 1, 1.1, 1.4, 1.8
H [m]	0.04

TABLE VII
OPERATIONAL AND EXTREME SEA STATE PARAMETERS TESTED DURING BASIN EXPERIMENTS

Operational Sea States	T_p [s]		H_{m0} [m]		γ
	full	model	full	model	
OSS 1	5.24	1.35	0.375	0.025	1.0
OSS 2	5.24	1.35	0.625	0.042	1.0
OSS 3	5.95	1.54	0.375	0.025	1.0
OSS 4	5.95	1.54	0.625	0.042	1.0
OSS 5	5.95	1.54	0.875	0.058	1.0
OSS 6	6.64	1.72	0.375	0.025	1.0
OSS 7	6.64	1.72	0.625	0.042	1.0
OSS 8	7.35	1.90	0.375	0.025	1.0
OSS 9	7.35	1.90	0.625	0.042	1.0
Extreme Sea States	T_p [s]		H_{m0} [m]		
	full	model	full	model	γ
ESS 1	3.03	0.782	0.495	0.033	1.0
ESS 2	5.00	1.29	1.02	0.068	1.0
ESS 3	7.35	1.90	1.5	0.100	1.8
ESS 4	8.75	2.26	2.65	0.175	3.3

* γ is the JONSWAP peak enhancement factor. In addition, a TMA correction [11] is applied to ESS 3 and 4.

C. Experimental configuration

The experiments were performed in the Model Test Basin at the Australian Maritime College (AMC). The wave basin is 35 m long and 12 m wide and the runs

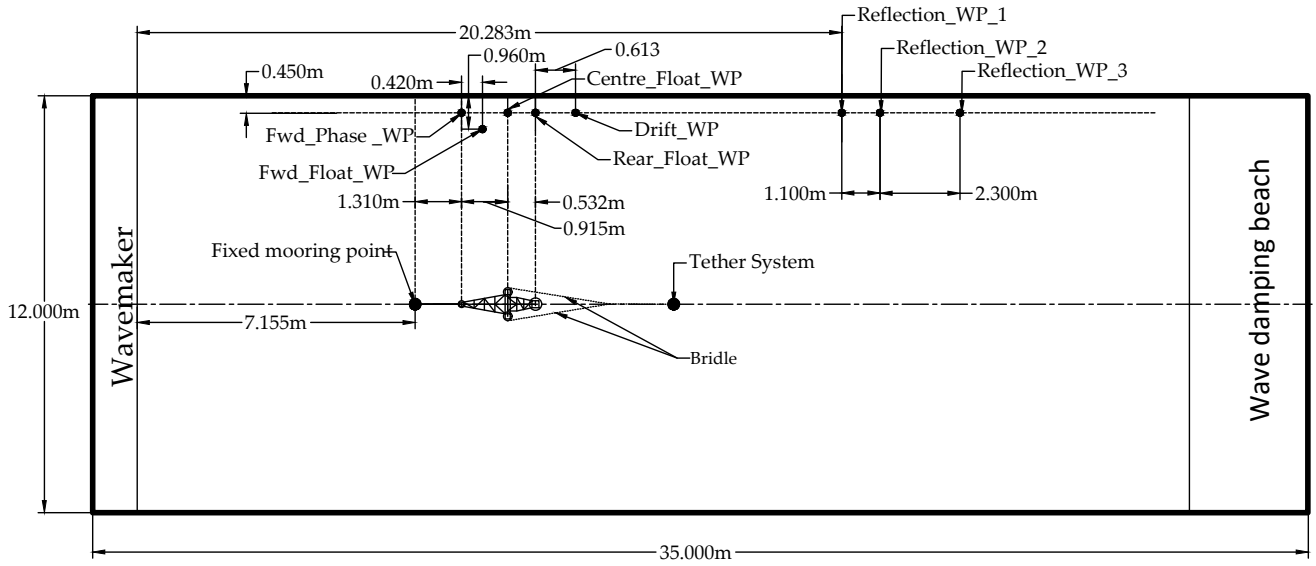

Fig. 6. Experimental configuration of the model in the AMC Model Test Basin.

were completed with a water depth of 0.8 m. Sixteen piston-type wave makers controlled by HR Merlin software was used to generate the wave conditions. The repeatability of the generated waves was confirmed during calibration of waves. Fig. 6 shows the layout of the wave basin with the position of the model and wave probes.

Eight wave probes were used to measure the surface elevation at different positions. Three probes were fixed in line with the position of the floats of the M4 model to estimate the surface elevation with respect to each float, one probe between the bow float and mid-float and another probe about 613 mm behind the rear float probe. Three probes were kept far behind the other probes to estimate the reflection from the passive absorber (beach).

The six degree-of-freedom (6-DOF) motions, and thus the hinge angle, of the M4 device were measured using Qualisys motion tracking technology. Four markers of 40 mm diameter were fixed on the forward part and four markers of 50 mm diameter were fixed on the aft body. This permitted Qualisys to track the motion of the forward body and aft body as independent rigid bodies; thus the hinge angle of the M4 device is computed as the relative pitch angle of the forward and the aft bodies.

Additionally, two cameras were used to record the response of the model. One camera was configured to record the global response of the model under wave excitation, while the second camera was configured with a focus on the mid floats of the model to capture the magnitude of any water run-up. Both the cameras recorded in 4K resolution at 25 fps and 97 VFR. These settings were selected such that the video playback of the model-scale tests could be observed at a full-scale temporal resolution in accordance with Froude scaling laws.

III. Results and discussion

The experimental test campaign of the M4 WEC generated a significant data set to aid in the characterisation of the device's performance in regular and irregular sea states. The combination of instrumentation utilised and conditions tested allows for analysis of parameters such as wave run-up on the PTO platform, performance in oblique seas, energy extraction in operational conditions and survivability in extreme sea states; however, these topics will be the focus of future works. The preliminary analysis presented in this study concerns the device's natural frequencies, the mooring stiffness, the PTO characteristics, motion response amplitude operators (RAOs) in regular and irregular seas and the reflection properties of the Australian Maritime College Model Test Basin during the experiments.

A. Model decay tests

A preliminary investigation was undertaken to experimentally evaluate the natural periods of the degrees of freedom of interest for the model, namely global heave, pitch and roll, along with the flex mode between the two rigid bodies. The Qualisys motion-tracking system was utilised to obtain temporal datasets for the respective degrees of freedom as each was tested in isolation. Fig. 7 illustrates an example of the decay time series for the flex mode of the model, which was derived as the difference between the independent pitch measurements for the two rigid bodies.

Fig. 7 details two independent tests: firstly where the central floats were forced downwards into submergence to create pitching of the two rigid bodies upon release, and secondly where the centre floats were raised upwards in the water column prior to being released for decay observation. It can be seen that there was good agreement in the natural decay

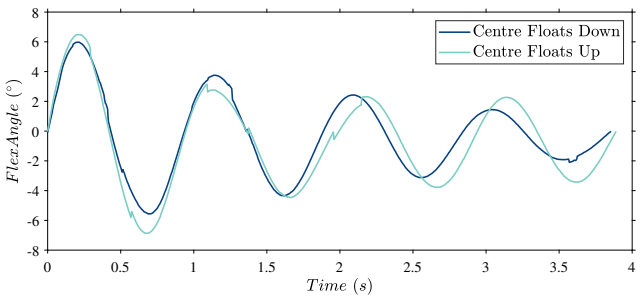

Fig. 7. Time series of M4 flex mode decay tests

period for the flex mode between the two tests, where the natural period was found to be 0.965 s and 0.973 s for the tests, respectively.

TABLE VIII
ESTIMATED AND EXPERIMENTALLY DERIVED NATURAL PERIODS FOR THE MODEL.

Mode	Predicted	Experimental
Flex [s]	0.84	0.97
Global Roll [s]	0.89	1.01
Global Pitch [s]	0.77	0.79
Global Heave [s]	0.76	0.78

The global heave, pitch and roll decay tests required the model to act as a single rigid body, which saw the implementation of a solid metal rod to replace the pneumatic ram and load cell (see Fig. 3), limiting any relative motion between the forward and aft arms. A summary of the natural periods of the model can be found in Table VIII, where predicted values, obtained from a linear numerical model described in [8], are also shown alongside the measured experimental values. The predicted values are the undamped and uncoupled natural periods of the respective modes.

B. Power take-off characterisation: Cyclic loading

The power take-off has been characterized through (non-cylic) extension and contraction tests as previously described, but the basin testing provides measurements of the actuator force and the hinge angle as the device responds to the waves. These measurements can be used to characterize the PTO in addition to the non-cyclic tests mentioned earlier. The extension and contraction of the actuator as a function of time are calculated from the measured hinge angle and the known equilibrium positions of the actuator's ends relative to the hinge. Differentiation with respect to time gives the velocity.

The behaviour of the actuator force under cyclic loading turns out to be highly nonlinear, as shown in Fig. 8, for example. The force-velocity profile suggests that the actuator force consists of not just linear viscous damping, but a combination of linear damping, Coulomb-type damping (with possibly unequal extension and contraction static frictions), and stiffness (as suggested by the hysteresis). Fig. 9 shows the actuator force time series from the regular wave run with 1 s

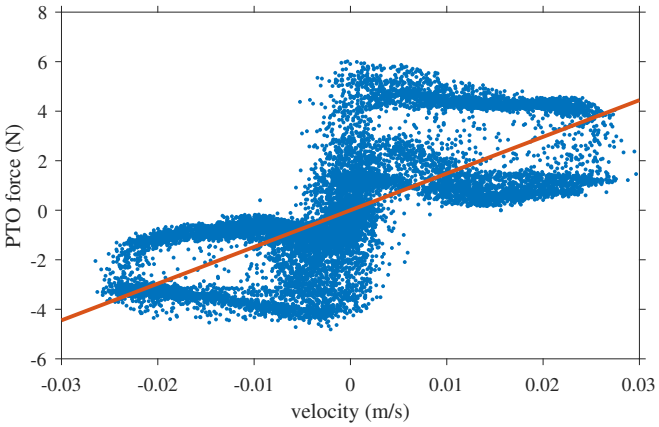

Fig. 8. Measured actuator force vs. velocity from regular wave test with a wave period of 1 s, and the least-squares linear fit (red).

period, i.e., corresponding to the plot in Fig. 8. A model which includes the aforementioned effects is shown in Fig. 10, which captures some of the prominent features of the measured force.

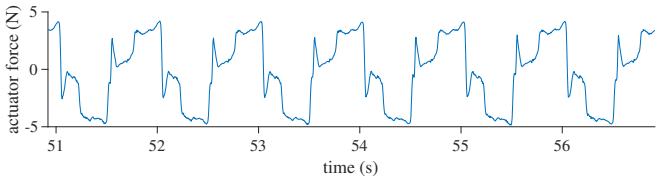

Fig. 9. Measured actuator force from regular wave test of 1 s period.

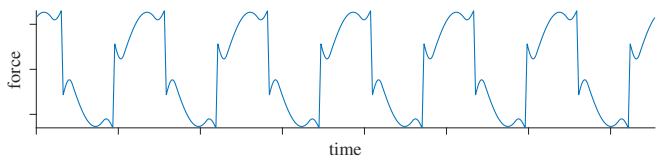

Fig. 10. Typical output of a PTO force model as a sum of linear viscous damping, linear stiffness, and an asymmetric Coulomb damping.

To accurately model such a complex behaviour would require a time-domain model with an accurate nonlinear representation of the PTO force. This is left as a future work. Nevertheless, for the present purpose of validating our linear numerical model, the data are fitted with a least-squares linear function, the slope of which gives the approximated linear damping coefficient.

Performing this fitting to the data from each of the regular wave runs, we find that the best-fit linear damping is a function of wave period (see Fig. 11). The damping coefficients identified from the contraction and extension tests (non-cyclic loading) prior to the wave tests are also shown for comparison. It is clear that for the longer wave periods (slow motion), the operating range of the actuator force is in the steep section of the force-velocity profile shown in Fig. 8, hence the much larger PTO damping coefficient.

While the load cell gives a force reading, a torque measurement is more useful since the Albany prototype will have a shaft connected to the hinge and both the torque and the hinge angle will be measured. For

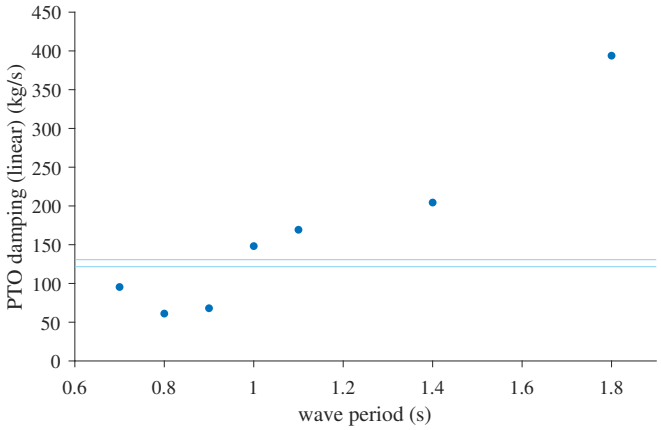

Fig. 11. PTO damping (linear) identified from regular wave tests. The two horizontal lines correspond to the damping identified from (non-cyclic) contraction and extension tests before the wave tests.

this reason, the measured actuator force is converted into torque by multiplying the force with the time-varying moment arm, which can be calculated from geometry and the measured hinge angle.

Performing the same fitting for the torque and angular velocity, we obtain the approximate angular damping coefficients shown in Fig. 12, as a function of wave period. The angular damping coefficient close to the natural period of the flex (relative pitch) mode is approximately 0.5 N·m·s, or about 100 kN·m·s at full scale.

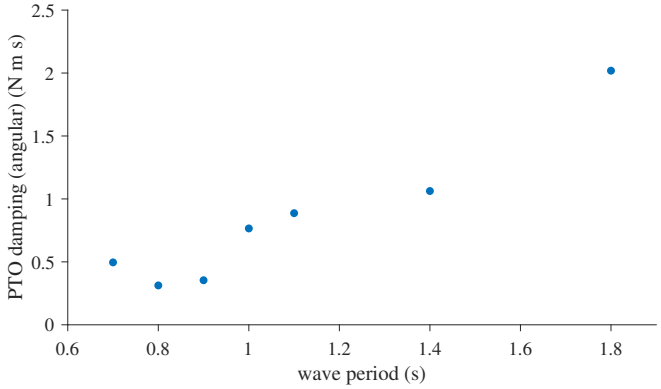

Fig. 12. PTO damping (angular) identified from regular wave tests.

It should be noted that the purpose of this exercise is to obtain an indication of the range of PTO damping across the different wave conditions tested, which, as Fig. 12 shows, is between 60 kN·m·s and 400 kN·m·s (full scale). Given the highly nonlinear nature of the actuator force, applying the best-fit linear damping to a linear numerical model to replicate the measured response to a regular wave of a specific wave period is not guaranteed to work. An agreement obtained using a damping coefficient that falls within the identified range would be deemed satisfactory. Some comparison examples will be reported in the following subsections.

C. Mooring force analysis

The mooring stiffness can also be estimated from the regular wave tests by finding the mean mooring force and the mean surge offset for the different regular wave runs. The force-offset pairs can be plotted as shown in Fig. 13. Linear regression gives a stiffness value of 4.88 N/m, which compares reasonably well with the stiffness value of 6.12 N/m measured before the test.

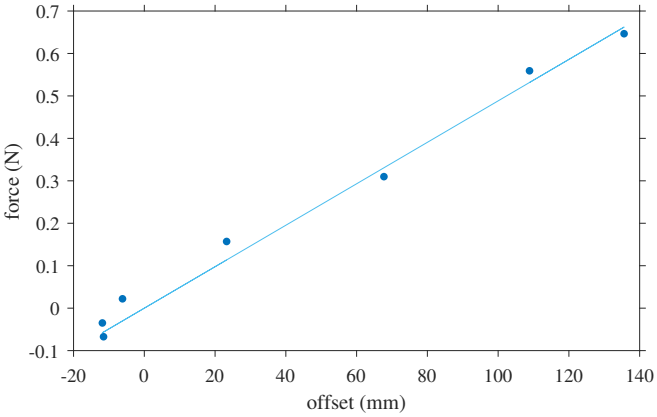

Fig. 13. Mean mooring force vs. mean surge offset identified from regular wave tests and the least-squares linear fit.

D. Motion response: Regular waves

The raw displacement data measured by the motion-tracking system were first processed before subsequent analyses were performed. This process involves, firstly, correcting the jumps in the data, which occur frequently in some of the degrees of freedom. An automated procedure is devised to perform this correction, which involves differentiating the raw signal, replacing the outliers, integrating it back, removing the drift of the resulting signal, and adding the drift of the original signal. The result has been found to be satisfactory; an example is shown in Fig. 14.

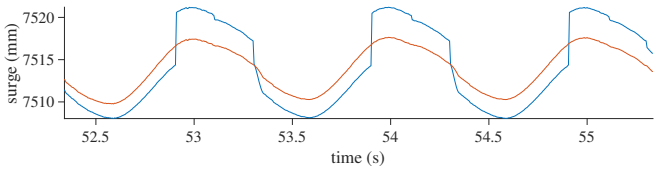

Fig. 14. Raw surge signal (blue) and the corrected time series (red), for regular waves of 1 s period.

Once the jumps have been corrected, the next step is obtaining the displacements at a chosen point of interest—in this case, the origin defined in the numerical model, for the purpose of comparing the measurements with the numerical predictions. The displacement data measured by the motion tracking system contain three translations and three rotations of each rigid body (forward and aft), hence 12 degrees of freedom in total, where only 7 of them are independent (since the aft body is constrained to the forward body by the hinges). The translations are defined as the Cartesian position of the local origin of each body relative to a global frame of reference, and the rotations as the orientation of the local axes relative to the global axes. To facilitate comparison with the numerical model predictions, the translations are transformed to

those at the numerical model's origin, which is located at the mean free surface, in the middle of the two mid floats.

Rather than using the full rotation matrix, a linear transformation is employed since the rotations of each body are rather small (less than approximately 20 degrees). This allows us to write the displacements of a point in the body as a sum of generalised modes [12]. Denoting the numerical model's origin as O, the position of a point $\mathbf{p}(t)$ in the global reference frame may be written as

$$\mathbf{p}(t) = \mathbf{p}_O + \mathbf{p}' + \sum \xi_i(t)\, \mathbf{S}_i(\mathbf{p}'), \tag{2}$$

where $\mathbf{p}_O$ is the equilibrium position of point O in the global reference frame, $\mathbf{p}'$ is the position of the same point relative to point O in the body frame (or when the body is at rest), $\xi_i(t)|i = 1, \ldots, 7$ are, respectively, the global surge, global sway, global heave, global roll, global pitch, global yaw, and the flex (relative pitch) modal displacements, and $\mathbf{S}_i$ is the shape function associated with mode i.

The position of point O in time,

$$\mathbf{p}_O(t) = \mathbf{p}_O + [\xi_1(t), \xi_2(t), \xi_3(t)]^\top, \tag{3}$$

can therefore be obtained from (2) if $\mathbf{p}(t)$, $\mathbf{p}'$ and $\xi_i|i = 4, \ldots, 7$ are known. In our case, the motion tracking system gives the positions $\mathbf{p}(t)$ of the local origins of the forward and aft bodies in the global frame, and their rotations, $\xi_i|i = 4, \ldots, 7$. Since the positions $\mathbf{p}'$ of the local origins relative to O are also known, the position of point O in time, $\mathbf{p}_O(t)$, can be calculated.

The shape function $\mathbf{S}_i(\mathbf{p}')$ gives the displacements of a point $\mathbf{p}'$ for a unit modal displacement, ξ_i. The shape functions $\mathbf{S}_i(\mathbf{p}')$ for surge, sway, and heave are simply the unit vectors in the respective directions, $\mathbf{i}, \mathbf{j}, \mathbf{k}$, whereas the shape functions for the rotational modes are given as

$$\mathbf{S}_4(\mathbf{p}') = -z'\mathbf{j} + y'\mathbf{k} \tag{4}$$

$$\mathbf{S}_5(\mathbf{p}') = z'\mathbf{i} - x'\mathbf{k} \tag{5}$$

$$\mathbf{S}_6(\mathbf{p}') = -y'\mathbf{i} + x'\mathbf{j} \tag{6}$$

$$\mathbf{S}_7(\mathbf{p}') = \begin{cases} (z' - z'_{\text{hinge}})\mathbf{i} - x'\mathbf{k} & \text{for } \mathbf{x} \in \text{aft body} \\ 0 & \text{elsewhere.} \end{cases} \tag{7}$$

Recall that $i = 7$ is the flex mode. Here, $\mathbf{p}' = (x', y', z')^\top$ is the position of the local origin relative to the numerical model's origin, O, and z'_{hinge} is the vertical coordinate of the hinge relative to O. The motion tracking system does not output ξ_7 directly but outputs the pitch of the aft body, ξ_{11}, from which ξ_7 can be obtained, by definition, from

$$\xi_7 = \xi_{11} - \xi_5. \tag{8}$$

Having obtained the displacements at point O, we choose a time window where the motion amplitudes are approximately steady. We then extract the first harmonics of the displacements within the chosen window.

Given that this window is relatively short (typically 5 to 6 wave periods), the extraction of the first harmonics is done by fitting a sinusoidal function having the same frequency as the wave frequency but with unknown amplitude and phase, casting this as a system of linear equations and obtaining the first-harmonic amplitude and phase as least-squares solutions. Fig. 15 shows an example of the first harmonic response time series from the regular wave test with a period of 0.9 s.

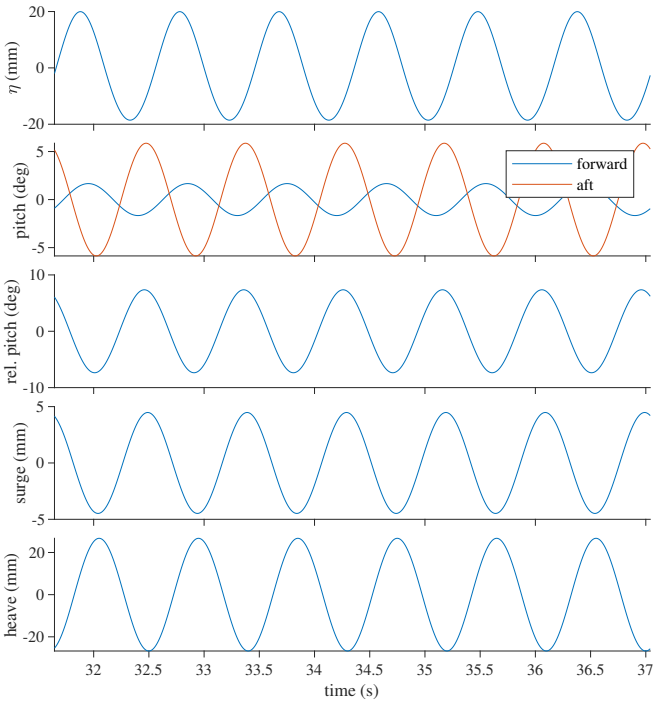

Fig. 15. Top to bottom: free-surface elevation at the wave gauge in line with the mid floats, pitch of the forward and aft bodies, hinge angle or relative pitch between the two bodies, surge and heave of the mid floats, in regular waves of 0.9 s period.

Certain features are evident from Fig. 15. As Table VIII shows, 0.9 s is close to the flex natural period, so we expect a large relative pitch response at around this period. The relative pitch is defined in (8) as the pitch of the aft body minus the pitch of the forward body, hence the negative relative pitch values approximately 90 degrees lagging the wave crests. The heave displacement is nearly 90 degrees lagging the surface elevation in line with the mid floats, implying that the mid floats are close to experiencing resonance.

E. Motion response: Irregular waves

Each of the irregular wave tests was run for a duration corresponding to approximately half an hour full scale, generating long-duration time series of the response, which makes it convenient to apply spectral analysis to derive response amplitude operators of the various responses. An example of the measured free-surface elevation, surge, heave and relative pitch response time series is shown in Fig. 16 for OSS 4.

This sea state represents the most frequently occurring sea state at the site, according to the joint probability diagram of significant wave height and mean wave period collected at the site [8]. The measured mean power (averaged from $t = 100$ s to $t = 400$ s to exclude the start and end portions) is 0.8 kW at full scale, in line with the numerically predicted mean power quoted in [8], i.e., 1.2 kW. The measured power has

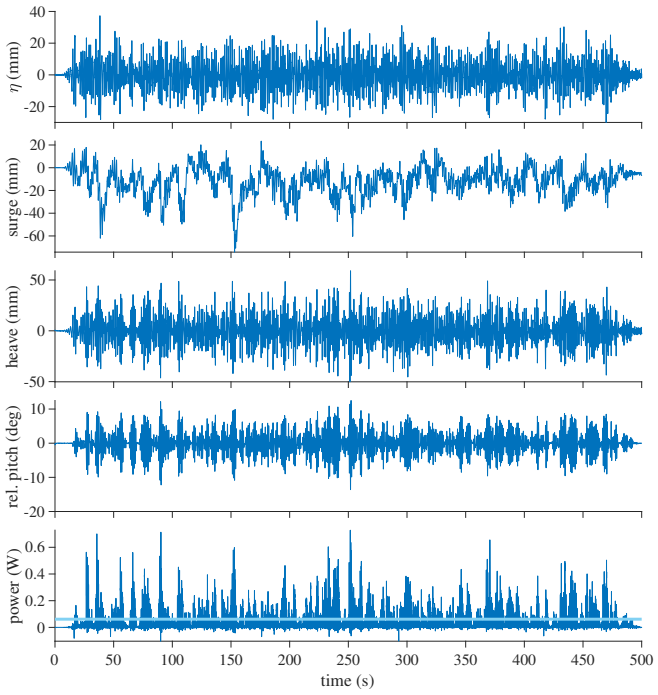

Fig. 16. Top to bottom: free-surface elevation at the wave gauge in line with the mid floats, surge, heave of the mid floats, relative pitch between the two bodies and measured power (with the mean as horizontal line), in operational sea state (OSS) 4.

been obtained as a product of the measured actuator force and the velocity of the ram.

The spectra of the free-surface elevations at all eight wave gauge positions are plotted in Fig. 17, showing good agreement with each other.

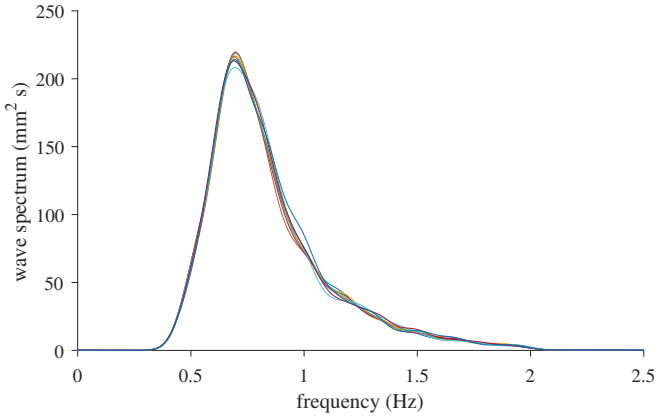

Fig. 17. Measured wave spectra from all eight wave gauges for OSS 4.

The RAO of a given response ξ is obtained as

$$\frac{\hat{\xi}(f)}{\hat{\eta}(f)} = \frac{S_{\eta\xi}(f)}{S_{\eta\eta}(f)}, \tag{9}$$

where $S_{\eta\xi}(f)$ is the cross-spectral density between the free-surface elevation as input and the response as output, $S_{\eta\eta}(f)$ is the spectral density of the free-surface elevation (shown in Fig. 17), and $\hat{}$ denotes the complex amplitude.

Fig. 18 shows the (absolute value) of these RAOs for the global surge, global heave, pitch of the two bodies, and relative pitch between the two. Two measurement lines are shown for the global surge and global heave RAOs. One line has been obtained by transforming the displacements of the forward body, and the other line was obtained using the aft body. The good agreement between the two indicates the transformation has been applied correctly.

Numerical predictions from the linear frequency-domain model described in [8] are overlaid in Fig. 18. An angular PTO damping coefficient of 200 kN·m·s has been used in the model. This value is close to the best-fit linear damping value seen in Fig. 12 for 1.1 s, which is the mean wave period of OSS 4. This PTO damping value works really well here, giving excellent agreement between the predicted and measured RAOs.

F. Reflection analysis

A preliminary analysis of reflection from the beach was undertaken for OSS 4. This made use of the reflection probes indicated in Figure 6 and the method of [13]. The analysis indicated that the beach reflection coefficient (in terms of amplitude) was less than 5% at the peak frequency (f_p) of the spectrum, and less than 20% when averaged over the range of the main energy-bearing components $0.7f_p < f < 2f_p$.

IV. Conclusions

Basin testing of the 1-2-1 M4 WEC has been detailed. The findings of this paper suggest good agreement between experimental results and numerical models that have been used in the design phase of the prototype to be deployed in King George Sound. Power absorption through a pneumatic ram is shown to be of the same order as expected power performance, though (perhaps inevitably) without the desired linear damping behaviour of the prototype. Additional analyses using this data will feed into preparations for the prototype deployment, including evaluation of run-up levels to site equipment on the WEC, mooring offsets in given seastates, and motion experienced on the access platform for personnel access.

Acknowledgement

The authors would like to thank the technical support team from the Australian Maritime College; in particular, Mr. Liam Honeychurch, Mr. Kye Curwen, Dr. Nick Johnson and Mr. Thomas Rehrmann for their assistance in construction of the model and facilitation of the experiments in the Model Test Basin.

References

[1] R. Moore, C. Murtagh, and B. Elaesser, "Design optimisation of an attenuator wave energy converter," in *Proc. of the 11th European Wave and Tidal Energy Conference, Nantes, France*, 2015.

[2] P. Stansby, E. Carpintero Moreno, T. Stallard, and A. Maggi, "Three-float broad-band resonant line absorber with surge for wave energy conversion," *Renewable Energy*, vol. 78, pp. 132–140, 2015.

[3] P. K. Stansby, E. Carpintero Moreno, and T. Stallard, "Modelling of the 3-float WEC M4 with nonlinear PTO options and longer bow beam," in *Progress in Renewable Energies Offshore: Proceedings of 2nd International Conference on Renewable Energies Offshore (RENEW2016)*, Lisbon, Portugal, October 2016, pp. 263–268.

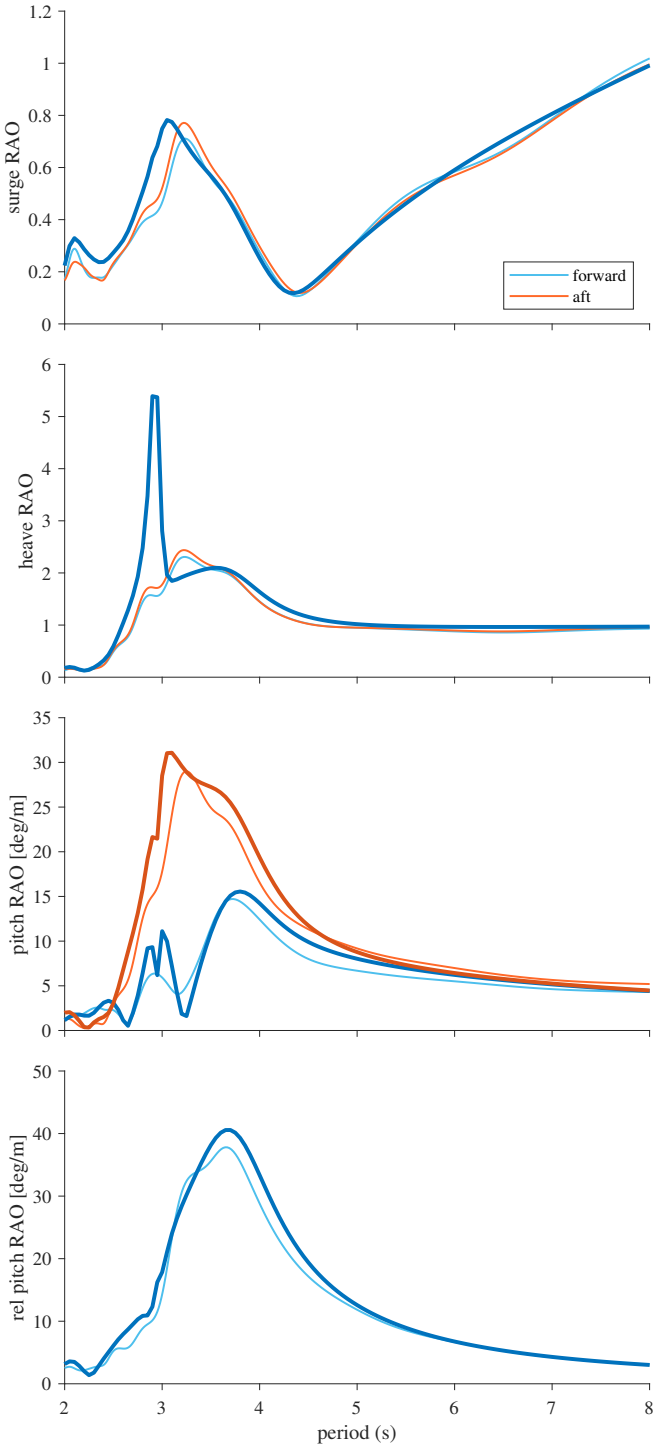

Fig. 18. Measured (thin lines) and predicted (thick) RAOs (full scale).

[4] P. K. Stansby, E. Carpintero Moreno, and T. Stallard, "Large capacity multi-float configurations for the wave energy converter M4 using a time-domain linear diffraction model," *Applied Ocean Research*, vol. 68, pp. 53–64, 2017.

[5] P. K. Stansby, E. Carpintero Moreno, and T. Stallard, "Capture width of the three-float multi-mode multi-resonance broadband wave energy line absorber M4 from laboratory studies with irregular waves of different spectral shape and directional spread," *Journal of Ocean Engineering and Marine Energy*, vol. 1, no. 3, pp. 287–298, Aug 2015.

[6] L. Sun, J. Zang, P. K. Stansby, and E. C. Moreno, "Performance of the three-float wave energy converter M4 in regular and random waves," in *Progress in Renewable Energies Offshore: Proceedings of the 2nd International Conference on Renewable Energies Offshore (RENEW2016)*, Lisbon, Portugal, October 2016, pp. 269–276.

[7] E. Carpintero Moreno and P. K. Stansby, "The 6-float wave energy converter M4: Ocean basin tests giving capture width, response and energy yield for several sites," *Renewable and Sustainable Energy Reviews*, vol. 104, pp. 307–318, 2019.

[8] A. Kurniawan, H. Wolgamot, C. Gaudin, C. Shearer, P. Stansby, and B. Saunders, "Numerical modelling in the development of the M4 prototype for Albany, Western Australia," in *Proceedings of the ASME 2023 42nd International Conference on Ocean, Offshore and Arctic Engineering*, Melbourne, Australia, June 2023.

[9] J. Apsley *et al.*, "Integrated hydrodynamic-electrical hardware model for wave energy conversion with m4 ocean demonstrator," in *Proceedings of the 15th European Wave and Tidal Energy Conference*, Bilbao, September 2023.

[10] C. L. Hansen, H. Wolgamot, P. H. Taylor, J. Orszaghova, A. Kurniawan, and H. Bredmose, "Design Wave analysis for the M4 wave energy converter," in *Proceedings of the 15th European Wave and Tidal Energy Conference*, Bilbao, September 2023.

[11] S. A. Hughes, "The TMA shallow-water spectrum description and applications," 1984.

[12] J. N. Newman, "Wave effects on deformable bodies," *Applied Ocean Research*, vol. 16, pp. 47–59, 1994.

[13] E. P. Mansard and E. Funke, "The measurement of incident and reflected spectra using a least squares method," in *Coastal Engineering 1980*, 1980, pp. 154–172.